Journal of Advanced Research 24 (2020) 353–361

Contents lists available at ScienceDirect

Journal of Advanced Research

journal homepage: www.elsevier.com/locate/jare

Half-life determination of inorganic-organic hybrid nanomaterials in mice using laser-induced breakdown spectroscopy

Yanwu Chu [a,1], Zhanjie Zhang [b,1], Qianyuan He [b], Feng Chen [a], Ziqian Sheng [a], Deng Zhang [a], Honglin Jin [b], Fagang Jiang [c,*], Lianbo Guo [a,*]

[a] Wuhan National Laboratory for Optoelectronics (WNLO), Huazhong University of Science and Technology, Wuhan, Hubei 430074, China
[b] Cancer Center, Union Hospital, TongjiMedical College, Huazhong University of Science and Technology, Wuhan, Hubei 430022, China
[c] Department of Ophthalmology, Union Hospital, Tongji Medical College, Huazhong University of Science and Technology, Wuhan 430022, China

GRAPHICAL ABSTRACT

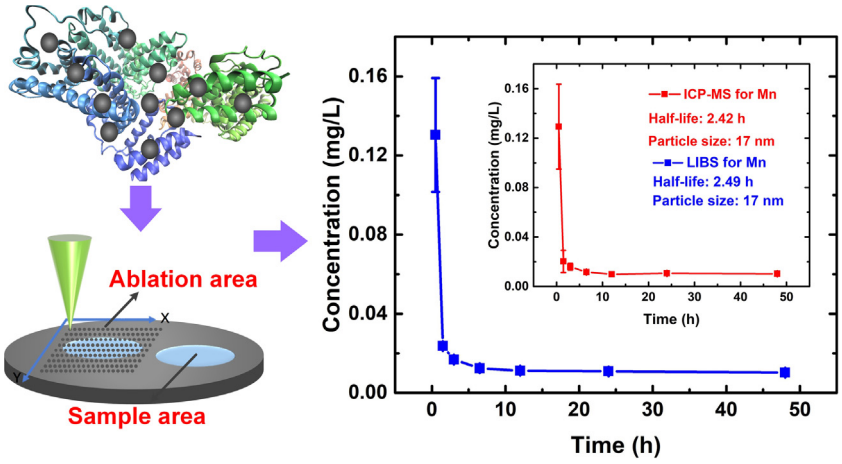

ARTICLE INFO

Article history:
Received 29 March 2020
Revised 24 April 2020
Accepted 1 May 2020
Available online 16 May 2020

Keywords:
Manganese dioxide-bovine serum albumin
Boehmite-bovine serum albumin
Laser-induced breakdown spectroscopy
Half-life detection

ABSTRACT

Inorganic or inorganic-organic hybrid nanomaterials have great potential for applications in the biomedical fields. Biological half-life is an essential pharmacokinetic parameter for these materials to function *in vivo*. Compared to inductively coupled plasma mass spectrometry (ICP-MS), which is the gold standard, laser-induced breakdown spectroscopy (LIBS) is a faster and more efficient elemental detection method. We investigated an efficient way to quantify the metabolic rate using LIBS. Nanoparticle platforms, such as manganese dioxide-bovine serum albumin (MnO_2-BSA) or boehmite-bovine serum albumin (AlO(OH)-BSA) were injected into mice through intravenous administration for LIBS spectrum acquisition. First, the spectral background was corrected using the polynomial fitting method; The spectral interference was eliminated by Lorentz fitting for each LIBS spectrum simultaneously. The support vector regression (SVR) was then used for LIBS quantitative analyses. Finally, the LIBS results were compared with the ICP-MS ones. The half-lives of MnO_2-BSA calculated by LIBS and ICP-MS were 2.49 and 2.42 h, respectively. For AlO(OH)-BSA, the half-lives detected by LIBS and ICP-MS were 3.46 and 3.57 h, respectively.

Peer review under responsibility of Cairo University.
* Corresponding authors.
E-mail addresses: fgjiang@hotmail.com (F. Jiang), lbguo@hust.edu.cn (L. Guo).
[1] These authors contributed equally to this work.

https://doi.org/10.1016/j.jare.2020.05.001
2090-1232/

The relative error of LIBS is within 5% compared to ICP-MS. The results demonstrate that LIBS is a valuable tool for quantifying the metabolic rates with a high degree of accuracy.

Introduction

Pharmacokinetics is the quantitative study of the absorption, distribution, metabolism, and excretion of drugs in organisms [1–3]. Proven pharmacokinetic properties are an important basis for judging the prospect of a drug in the market. Half-life is an important pharmacokinetic parameter and refers to the concentration of drugs in the blood or the time it takes for the amount of drugs in the body to decrease to one-half [4,5]. Half-lives determines the number of doses, intervals, the first dose, and maintenance dose. The half-lives of different drugs vary greatly. Therefore, it is important to detect the half-lives of drugs accurately and rapidly.

Bovine serum albumin (BSA), a multifunctional biocompatible drug delivery carrier, can isolate inorganic ions through biomineralization to form protein-coated metal oxide nanoclusters under alkaline conditions [6–8]. Manganese dioxide-bovine serum albumin (MnO_2-BSA) is a promising biomimetic catalyst for water oxidation and is synthesized using BSA as a template through biomineralization [9,10]. The nanoparticles synthesized by this method have strong biocompatibility. The single-particle-diameter of the nanoparticles is about 20 nm, which benefits the long-term circulation of the nanoparticles in an organism. Boehmite (AlO(OH)) has unique chemical, optical, and mechanical properties and has been widely used in carriers, semiconductors, and composite materials [11]. Both nanomaterials with excellent chemical properties have broad prospects for applications. Therefore, it is clinically important to detect the half-lives of these inorganic-organic hybrid nanomaterials, including MnO_2-BSA and AlO(OH)-BSA.

The most commonly used technique for determining the half-lives of drugs is inductively coupled plasma mass spectrometry (ICP-MS) [12–14]. J.G. Morrison *et al.* detected platinum in biometrics at a low level using ultrasonic nebulization coupled with ICP-MS [15]. ICP-MS is accurate and robust, but its sample preparation is tedious, time consuming, and expensive. Hence, it is vital to develop a faster and more economical technology for determining the half-lives of drugs.

Laser-induced breakdown spectroscopy (LIBS), an emerging field-portable sensor technology, has many advantages over traditional element detection technology [16–18]. The advantages of LIBS include rapid detection, no pretreatment of samples, and real-time analysis [19,20]. It can be applied to many elemental analysis occasions such as food safety identification [21–23], industrial monitoring [24,25], and environmental detection [26,27]. LIBS technology has been employed for liquids detection in the field of water pollution, such as detection of heavy metal pollution in water [28–31]. There have been two main methods for the detection of liquid using LIBS [32,33]. One is direct detection. F. Y. Yueh *et al.* directly measured trace elements in a column of liquid, and the lowest limit of detection (LOD) was 0.1 ppm [34]. The other method utilizes the surface enhancement effects to detect metal elements in liquids. Aguirre et al first proposed the surface-enhanced LIBS (SENLIBS) method for element analysis, and the LOD of Mn was 6 μg/g. [32]. Collectively, the studies described above prove that LIBS can meet the requirement of detecting a metal element in a liquid. In most cases, compared to ICP-MS, the detection cost and time of LIBS are much lower. To date, few works have been conducted using LIBS for detecting half-lives of the nanomaterials. To our knowledge, the application of LIBS in determining the half-lives of inorganic-organic hybrid nanomaterials, such as MnO_2-BSA and AlO(OH)-BSA, has not been reported.

In this study, the inorganic-organic hybrid nanomaterials (MnO_2-BSA and AlO(OH)-BSA) were successfully synthesized. The half-life of the MnO_2-BSA/AlO(OH)-BSA was quantified in mice using LIBS combined with a polynomial fitting for background removal and a Lorentzian fitting for spectral interface elimination, respectively. The half-lives determined by ICP-MS were compared with the LIBS ones. The quantitative analysis performance was evaluated using the coefficients of determination (R^2) and root mean squared errors (RMSE).

Fundamental materials and methods

Half-lives

Drug half-lives refer to the times required a drug concentration to drop to half. The half-life can be used to determine the dosing interval and dose. Body volume can also be estimated by half-lives. In this work, the average steady-state concentration was

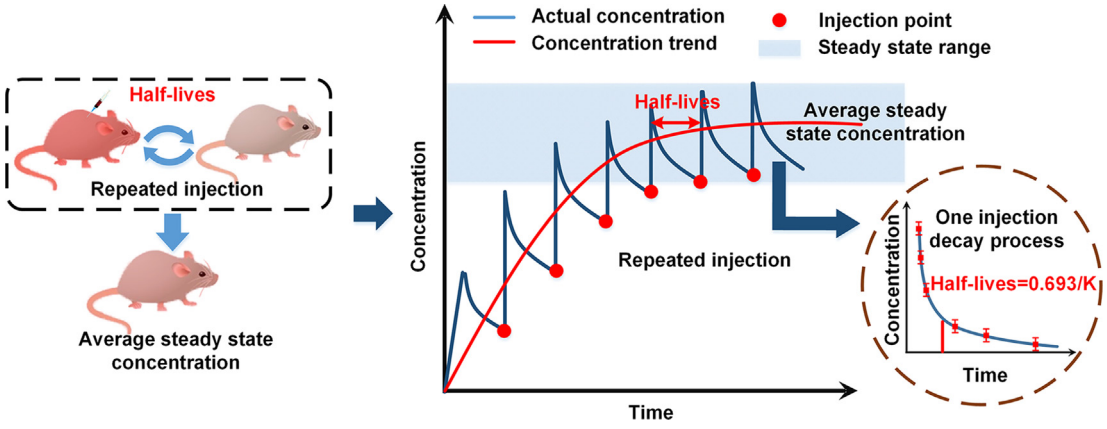

Fig. 1. Drug concentration change processes after repeated injections. The whole process of concentration changes after one injection.

obtained by repeated injections. A diagram of the drug concentration change process after repeated injections is shown in Fig. 1. The half-lives can be calculated by concentration changes after each injection.

Synthesis of MnO_2-BSA nanoparticles

Bovine serum albumin (BSA), potassium permanganate ($KMnO_4$), sodium hydroxide (NaOH), and hydrogen peroxide (H_2O_2) were all purchased from Aladdin (China). The MnO_2-BSA nanoplatforms were synthesized via a facile procedure. In brief, 7 ml of $KMnO_4$ (10 mmol/l in the ultrapure water) was added by drops into a 30 ml BSA solution (10 mg/ml in the ultrapure water). Subsequently, the mixture was stirred overnight at room temperature until the color changed from fuchsia to dark brown, which indicates that the $KMnO_4$ was completely reduced to MnO_2. Finally, the synthetic MnO_2-BSA was washed three times with double-distilled water using a dialysis bag (molecular weight cut-off: 8–14 kDa). The MnO_2-BSA was dispersed again in water and stored at 4 °C for further use.

Synthesis of AlO(OH)-BSA nanoparticles

Synthesis of AlO(OH)-BSA. The AlO(OH) nanoparticles were obtained using a method previously reported with slight modifications. First, 20 ml of $[Al(NO_3)_3{\cdot}9H_2O]$ solution (69.6 mg/ml in ultrapure water) and 0.393 ml of ethylenediamine (EDA) were added to a 50 ml glass vial with continuous stirring. Subsequently, the mixture was transferred into a stainless-steel autoclave and maintained at 250 °C for 24 h. When the reaction was completed, the resulting AlO(OH) nanoparticles were separated by centrifugation and washed several times with ethyl alcohol and ultrapure water to remove all ionic remnants. The purified AlO(OH) nanoparticles were stored at 4 °C before dispersed in water and mixed with BSA (10 mg each). The solution was then vigorously mixed at room temperature for 12 h. Finally, the AlO(OH)-BSA was obtained by filtering the reaction liquid with 100-kDa filters.

Sample pretreatment

After the MnO_2-BSA and AlO(OH)-BSA were successfully prepared, the same concentration of phosphate buffer saline (PBS) solution was prepared as the injections for the control group. A schematic diagram of the sample processing is shown in Fig. 2 (a). The details of the pretreatment steps are described below:

(1) The experimental samples consisted of two groups of three mice each, and 300 μl MnO_2-BSA and AlO(OH)-BSA with a concentration of 0.5 mg/ml was injected separately into three mice. The same dose of PBS was injected into the control group.
(2) A pipette was used to obtain 10 μl of blood from each mouse by shearing tail at time intervals of 0.5, 2, 2.5, 6.5, 10.5, 24, and 48 h after injections.

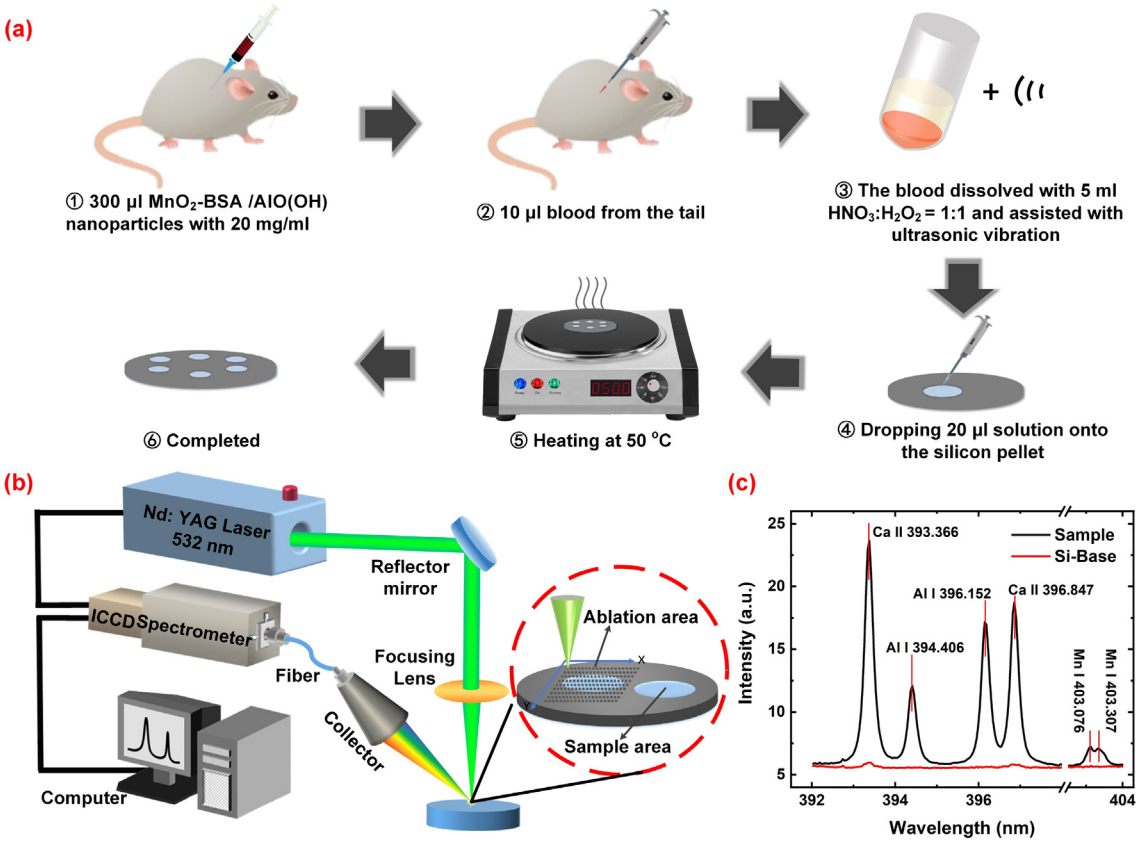

Fig. 2. (a) Schematic diagram of sample processing. ① drug injection of a certain dose of; ② take 10 μl of blood to avoid the impact of blood on the mice; ③ dissolve blood using ultrasonic shock for 5 min; ④ drop 20 μl of dissolved liquid onto a silicon pellet surface; ⑤ heated for 2 min to accelerate evaporation; and ⑥ sample processing is completed directly for LIBS detection. (b) Schematic diagram of the LIBS system including a laser, a spectrometer, and a high-precision three-dimensional platform. The spectrometer is triggered directly by the laser, and the laser ablation area is larger than the sample area to overcome the coffee ring effect. (c) LIBS spectrum of serum sample and Si-Base at a band of 392–404 nm.

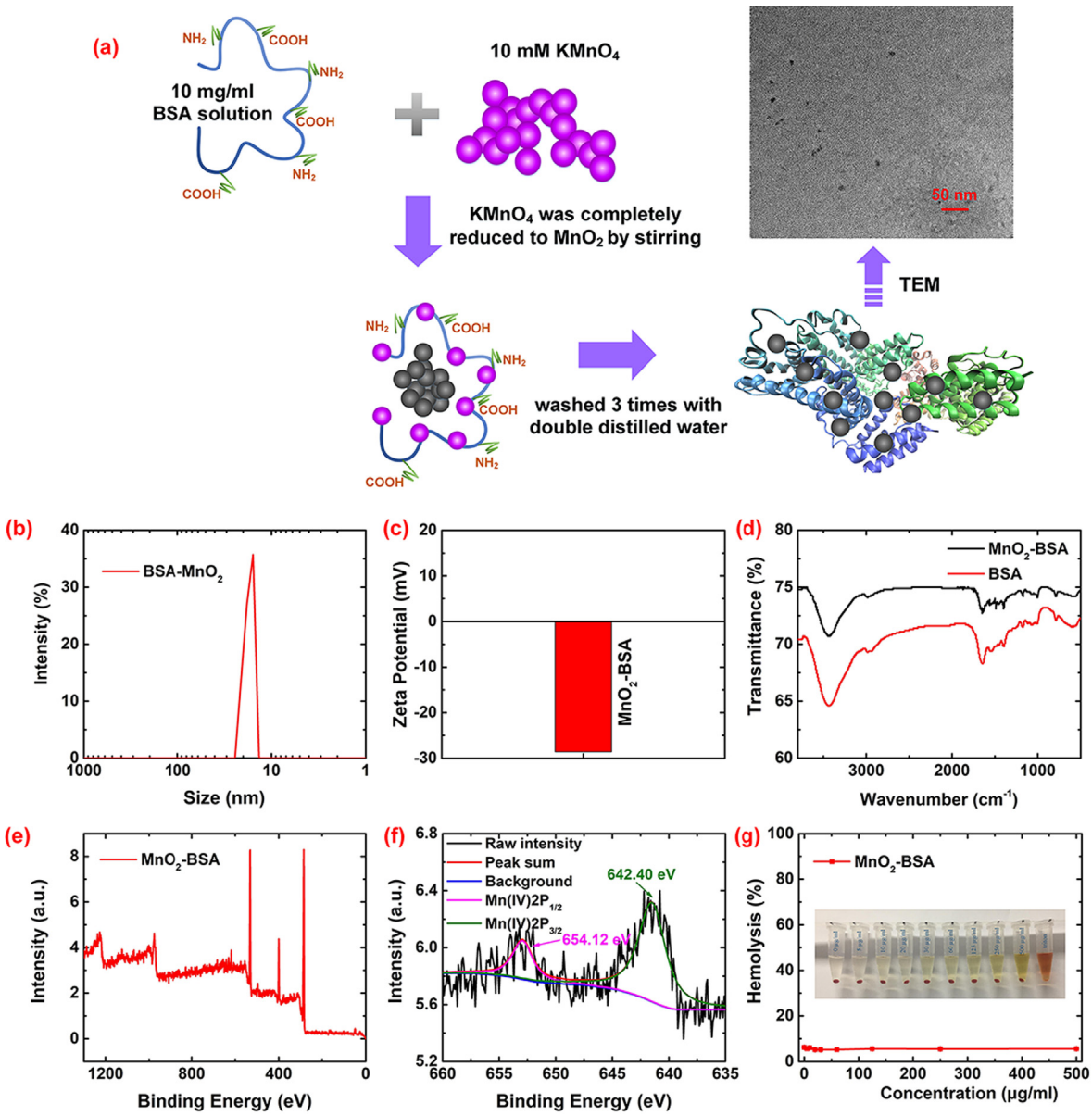

Fig. 3. The characterization of MnO_2-BSA: (a) schematic diagram of the synthesis of MnO_2-BSA and the TEM image of MnO_2-BSA, (b) the hydrodynamic size distribution of MnO_2-BSA detected by DLS, (c) the zeta potential of MnO_2-BSA, (d) the IR spectrum of MnO_2-BSA, (e) the X-ray photoelectron spectrum in the band of 0–1200 eV, (f) two characteristic absorption peaks of Mn(IV) $2P_{1/2}$ and $2P_{3/2}$ detected by XPS, and (g) hemolytic assay for MnO_2-BSA at different concentrations with triton (1%) as a positive control (100% hemolysis, the first from right).

(3) The 10 μl blood samples were mixed with a 5 ml solvent of nitric acid and hydrogen peroxide with a ratio of 1:1 by ultrasonic shaking in an ultrasonic cleaner for 5 min.
(4) A 20 μl solution was dropped onto a silicon pellet using a micropipette. The silicon pellet was placed on a heater at 50 °C for 2 min to obtain sample.

LIBS experimental setup

A schematic diagram of the LIBS spectrum acquisition is shown in Fig. 2(b). The two main instruments of the system were a Q-switched Nd: YAG laser (French Quantel Ultra 100; wavelength: 532 nm; pulse energy: 3.6 mJ; pulse duration: 7 ns; repetition rates: 10 Hz) and a Czerny-Turner spectrometer (United Kingdom, Andor Technology, Shamrock 500, input side slit width: 100 μm, grating groove densities: 1200 lines/mm) equipped with an intensified charge-coupled device (ICCD) (United Kingdom, Andor Technology, iStar 320 T). In an open air, the laser beam was reflected by a dichroic mirror and then focused onto the sample surfaces by an ultraviolet (UV)-grade quartz lens (f = 25 mm) to produce plasma. To avoid the formation of a deep crater, the sample was mounted on a motorized XYZ translation stage at a speed of 1 mm/s. The laser beam scanned the sample in a rectangle trace. To maximize the signal-to-noise ratio, the spectra were acquired at an optimized delay time of 3 μs with a gate width of 5 μs. Each spectrum was accumulated for ten shots and repeated ten times to reduce the intensity deviation. The diameter of spot size was about 300 μm. The LIBS spectrum at a band of 392–404 nm is shown in Fig. 2 (c). There are no interference spectral lines for manganese (Mn) and Aluminum (Al) in the silicon pellet.

Results and discussion

Material characterization

The schematic diagram of synthesizing MnO_2-BSA and the transmission electron microscope (TEM) image of MnO_2-BSA are shown in Fig. 3(a). As shown in the TEM image, a spherical nanoparticle was synthesized in this experiment. The results of dynamic light scattering (DLS) are shown in Fig. 3(b) to indicate that the hydrated particle diameter of MnO_2-BSA was about 17 nm, which is consistent with the TEM results. These results proved that MnO_2-BSA was successfully synthesized. Fig. 3(c) shows that the zeta potential of MnO_2-BSA is −28.2 ± 4.7 mV using a nanoparticle analyzer. The strong negative charge can prevent MnO_2-BSA from being rapidly removed by phagocytic cells *in vivo* and increase the blood circulation cycle of MnO_2-BSA. The infrared (IR) absorption spectroscopy are shown in Fig. 3(d). The spectrum indicates that there are absorption peaks at 1658 and 1533 cm^{-1}, respectively, in MnO_2-BSA, which are the stretching vibration of carbonyl and the bending vibration of the N-H imines in the amide bond indicating the presence of BSA in the nanoparticles. As revealed by the X-ray photoelectron spectroscopy (XPS) analysis (Fig. 3(e-f)), there are two characteristic absorption peaks at 654.2 and 642.4 eV, which are the Mn (IV) $2p_{1/2}$ and $2p_{3/2}$ of the spin-orbit peaks for MnO_2, respectively, confirming the presence of MnO_2 in the nanoparticles. The hemolytic assay results of MnO_2-BSA are shown in Fig. 3(g). At a concentration of 500 μg/ml of MnO_2-BSA, the hemolysis rate was 5.6%, indicating that it has strong biocompatibility.

The schematic diagram of synthesizing AlO(OH)-BSA and the TEM image of AlO(OH)-BSA are shown in Fig. 4(a). As shown in

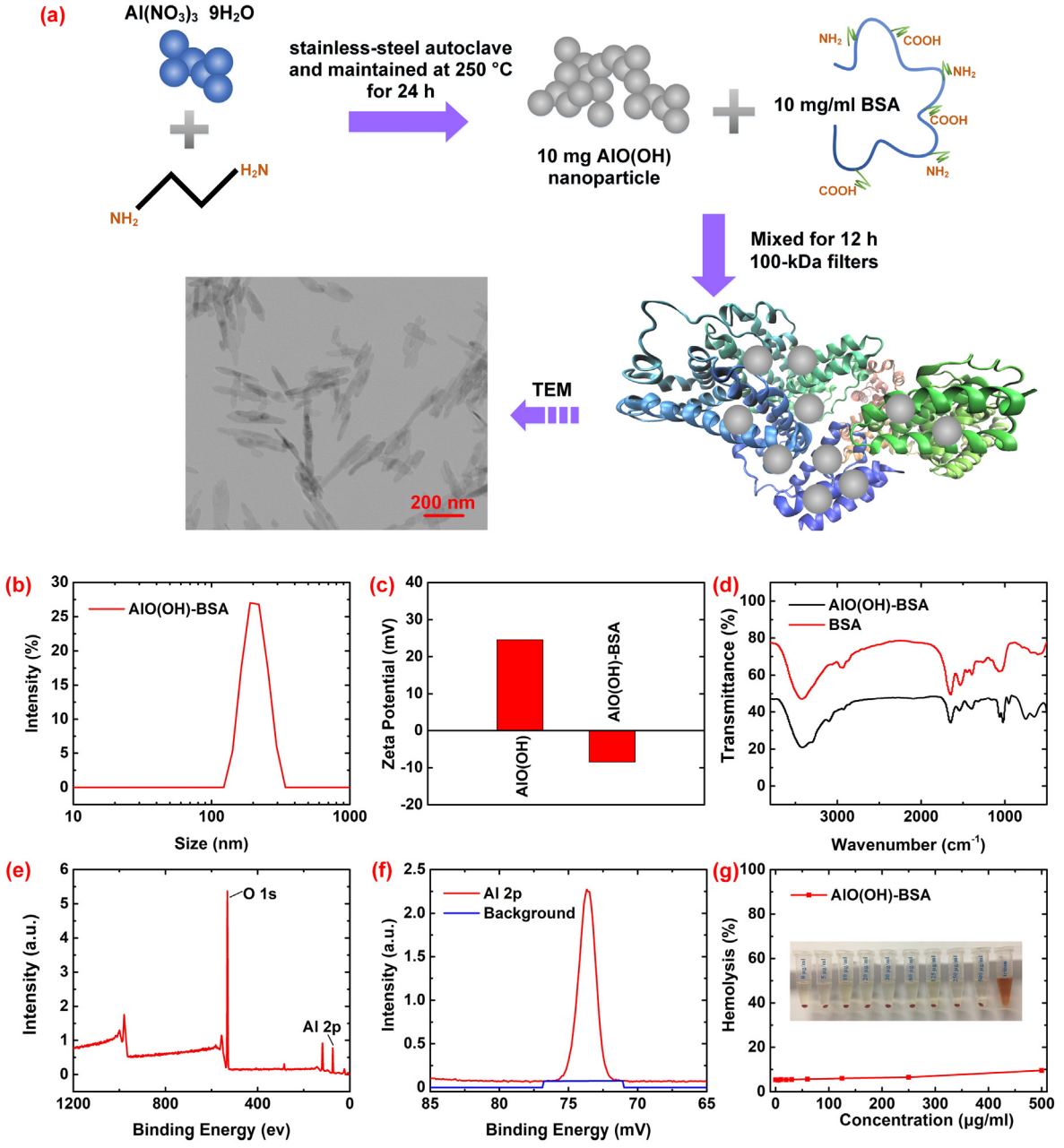

Fig. 4. The material characterization of AlO(OH)-BSA: (a) schematic diagram of the synthesis of AlO(OH)-BSA and the TEM image of AlO(OH)-BSA, (b) the hydrodynamic size distribution of AlO(OH)-BSA detected by DLS, (c) comparison of the zeta potential of AlO(OH) and AlO(OH)-BSA, (d) the IR spectra of AlO(OH)-BSA and BSA, (e) the XPS spectrum in the band of 0–1200 eV, (f) a characteristic absorption peak of Al 2p in XPS, and (g) hemolytic assay for AlO(OH)-BSA at different concentrations with triton (1%) as a positive control (100% hemolysis, the first from right).

the TEM image, the nanoparticles synthesized are rod-shaped. From the DLS data shown in Fig. 4(b), the hydrated particle size of AlO(OH)-BSA is about 200 nm, which is in agreement with the TEM results. Fig. 4(c) shows that the zeta potential of AlO(OH)-BSA is −8.47 ± 3.2 mV. The negative charge can prevent AlO(OH)-BSA from being cleared by phagocytic cells *in vivo* and prolonging the blood circulation cycle of AlO(OH)-BSA. IR spectra of AlO(OH)-BSA and BSA are shown in Fig. 4(d). The characteristic stretching vibration of the amide and the bending vibration characteristic peaks of N-H in the secondary amine are detected at 1658 and 1533 cm^{-1}, indicating the existence of BSA in AlO(OH)-BSA. XPS spectra are shown in Fig. 4(e-f). As shown in Fig. 4(f), the Al 2p characteristic absorption peak is at 74.6 eV, suggesting the successful loading of AlO(OH) into the nanoparticles. The hemolytic assay results of AlO(OH)-BSA are shown in Fig. 4(g). For AlO(OH)-BSA at a concentration of 500 μg/mL, the hemolysis rate is 9.6%, which means it has strong biocompatibility.

Spectral pretreatment

After the successful synthesis of MnO_2-BSA and AlO(OH)-BSA, they were injected into the mice. Blood samples were collected at different time intervals. The blood samples were dissolved using a mixed solvent of nitric acid and hydrogen peroxide for LIBS detection. With the experimental setup and acquisition parameters described above, the LIBS spectra of the samples were obtained. Both Al and Mn in the band of 392–404 nm are affected by background signal and spectral interference. The correlation coefficient between intensity of Mn I 403.307 and Mn I 403.377 and the concentration of Mn were 0.988 and 0.985, which means Mn I 403.307 is better analytical line. The Mn I 403.307 and Al I 394.406 were interfered by Mn I 403.377 and Ca II 393.377, respectively. The spectral interference of Mn is more obvious. The background signal was corrected by polynomial fitting. Background signal includes bremsstrahlung radiation and electron-ion complex radiation. The secondary term was used to fit the bremsstrahlung radiation which is inversely proportional to the square of the wavelength. The third order term is used to fit the nonlinear electron-ion complex radiation. The spectral interference was eliminated by Lorentzian fitting. The full width at half maximum and peak intensity of the spectrum are used as the initial values of the Lorentzian fitting. The algorithm flowchart for spectral pretreatment is shown in Fig. 5(a). The pretreatment results of the MnO_2-BSA and AlO(OH)-BSA blood solution spectra are shown in Fig. 5(b-d) and (e-f), respectively. To improve the quantitative analyses of Mn I 403.076 and Al I 394.4 nm, the background signal and the spectral lines were corrected by the proposed method. After polynomial fitting and Lorentzian fitting, the R^2 of the fitting between the sum of background signal, interference line, and analysis line and the original spectrum for Mn I 403.076 and Al I 394.406 nm are 0.9910 and 0.9927, respectively.

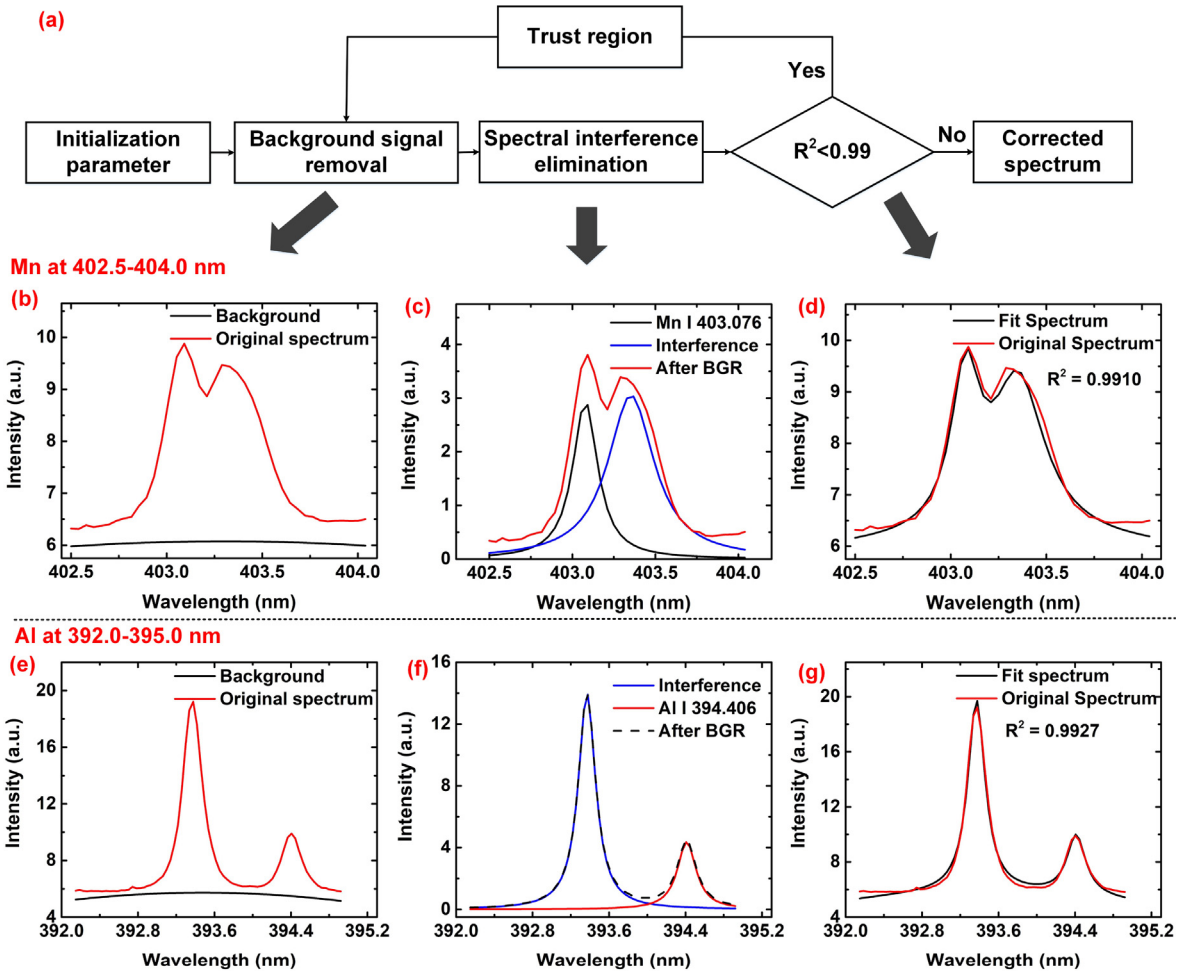

Fig. 5. (a) Algorithm flowchart for spectral pretreatment. (b) Cubic polynomial fitting to calculate spectral background for the band of 402.5–404 nm. (c) Lorentzian fitting divides the spectrum after background removal into interference line and Mn I 403.076 line. (d) Comparison of the original spectrum and curve fitting line which is the sum of background, interference line, and Mn I 403.076 line. (e) Cubic polynomial fitting to calculate spectral background for the band of 392–395 nm. (f) Lorentzian fitting divides the spectrum after background removal into interference line and Al I 394.406 line. (g) Comparison of the original spectrum and curve fitting line which is the sum of background, interference line, and Al I 394.406 line.

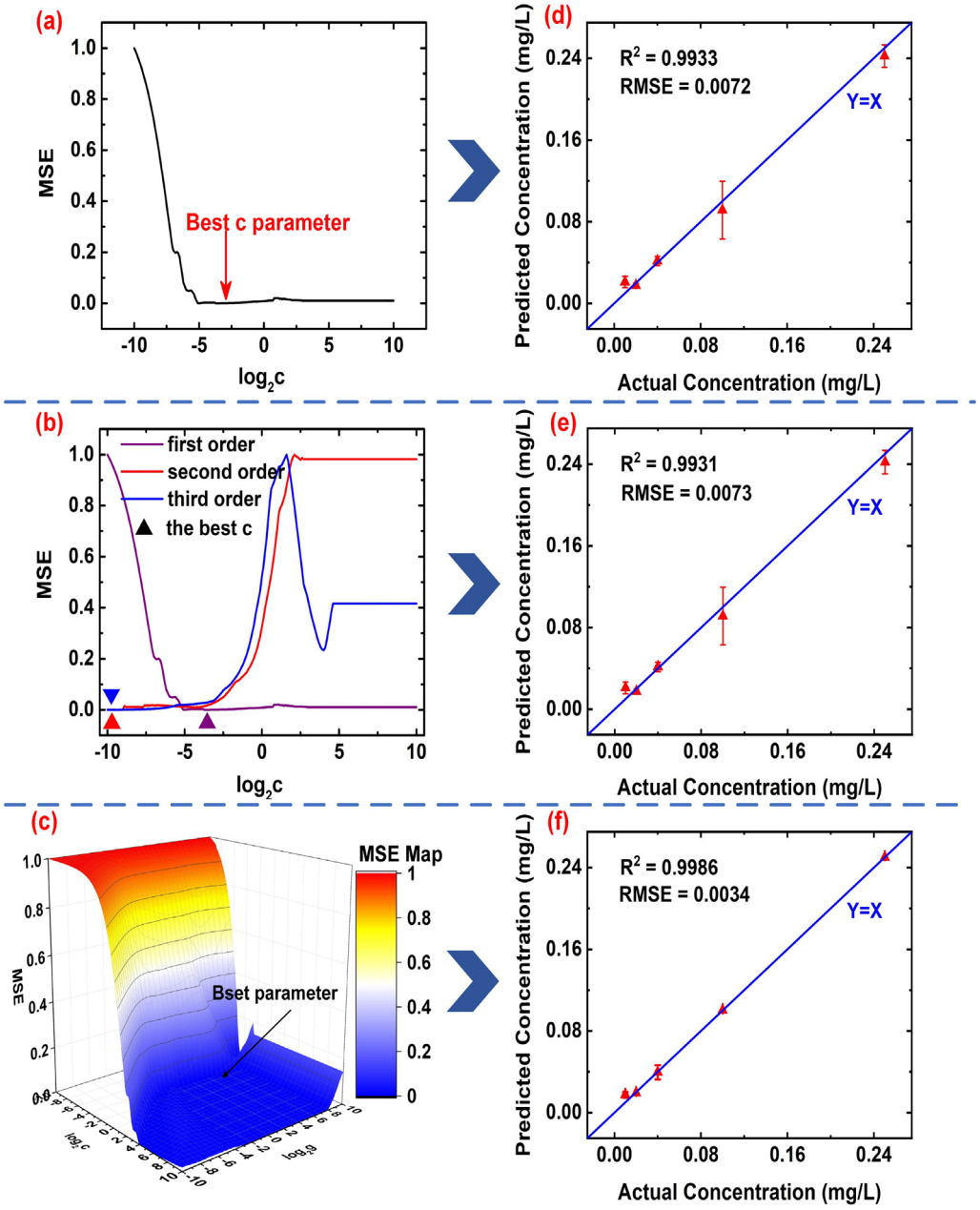

Fig. 6. (a) The optimization results for the penalty parameter *c* for linear function at Mn I 403.076; (b) the penalty parameter *c* and the optimization result for order parameter *d* for polynomial function at Mn I 403.076; (c) the penalty parameter *c* and the gamma parameter *g* optimization result for RBF function at Mn I 403.076. (d) the predicted concentration and the actual concentration of Mn using the SVR model based on linear function; (e) the predicted concentration and the actual concentration of Mn using the SVR model based on polynomial function; and (h) the predicted concentration and the actual concentration of Mn using the SVR model based on RBF function.

Quantitative analyses of LIBS and ICP-MS

For the quantitative analyses using LIBS, a calibration curve was established using a solution with a concentration gradient of 0.01, 0.02, 0.04, 0.10, and 0.25 mg/l for Mn and Al. After the LIBS spectra acquisition, the original spectra were corrected by the proposed pretreatment method for background remove and interference elimination. The corrected spectra at the band of 402.5–404 nm and 392–395 nm were input into the multivariate analysis model such as the support vector regression (SVR) model and the partial least-square regression (PLSR) model for quantitative analyses of Mn and Al, respectively. The SVR model was used for quantitative analysis of the Mn and Al elements. The SVR model was built using the Library for Support Vector Machines (LIBSVM) toolbox [35]. The penalty parameter *c* needs to be optimized for three kinds of kernel functions. The order parameter *d* and the gamma parameter *g* were optimized for the polynomial kernel function and radial basis function (RBF). The parameter optimizations for three kinds of kernel functions are shown in Fig. 6(a-c). The results of Mn quantitative analysis of the linear, polynomial, and RBF function are shown in Fig. 6(d-f), respectively. For both kinds of drugs, the SVR model based on the RBF kernel functions has the best quantitative analysis performance. The best R^2 and RMSE of the SVR model for Mn were 0.9986 and 0.0034, respectively. The best R^2 and RMSE of the SVR model for Al were 0.9978 and 0.0042, respectively. The R^2 and RMSE of the SVR model, The PLSR model, and calibration curve for Mn and Al are listed in Table 1.

Table 1
Comparison of quantitative analysis results.

	Mn-R^2	Mn-RMSE	Al-R^2	Al-RMSE
Calibration curve	0.9941	0.0088	0.9920	0.0080
PLSR	0.9984	0.0035	0.9969	0.0049
Linear-SVM	0.9933	0.0072	0.9969	0.0049
Polynomial-SVM	0.9931	0.0073	0.9970	0.0048
RBF-SVM	**0.9986**	**0.0034**	**0.9978**	**0.0042**

The LIBS quantitative analyses model was built using the SVR model. The concentrations of MnO_2-BSA and AlO(OH)-BSA at seven time point can be calculated by the SVR model. The samples to be tested were also quantitatively analyzed by ICP-MS. The comparison of the detection results of the MnO_2-BSA and AlO(OH)-BSA concentrations changing with time are shown in Fig. 7(a-b) and (c-d), respectively. As expected, LIBS and ICP-MS detection results have the same trend for both nanomaterials. The detection results of both LIBS and ICP-MS are listed in Table 2. The mean relative error of seven time points between the results of both LIBS and ICP-MS were 5.65% and 2.63%, respectively. The comparison of quantitative analysis results between LIBS and ICP-MS are listed in Table 2. For MnO_2-BSA, the half-lives were 2.42 ± 0.087 and 2.49 ± 0.103 h, respectively, using ICP-MS and LIBS. The half-lives of AlO(OH)-BSA were 3.57 ± 0.495 and 3.46 ± 0.480 h using ICP-MS and LIBS, respectively. The half-life of AlO(OH)-BSA is longer than MnO_2-BSA due to the larger particle size, as shown in the TEM image.

Conclusions

This work was to detect the metabolic rates of inorganic-organic hybrid nanomaterials using LIBS to achieve simple, efficient, and low-cost half-life detection with MnO_2-BSA and AlO(OH)-BSA for concept models. The MnO_2-BSA and AlO(OH)-BSA were successfully synthesized and characterized by TEM, IR, and XPS. The original LIBS spectra were corrected by the polynomial and Lorentzian fittings. The SVR model based on the RBF kernel function has the best quantitative analysis performance. The R^2 and RMSE of LIBS detection combined with SVR are 0.9941 and

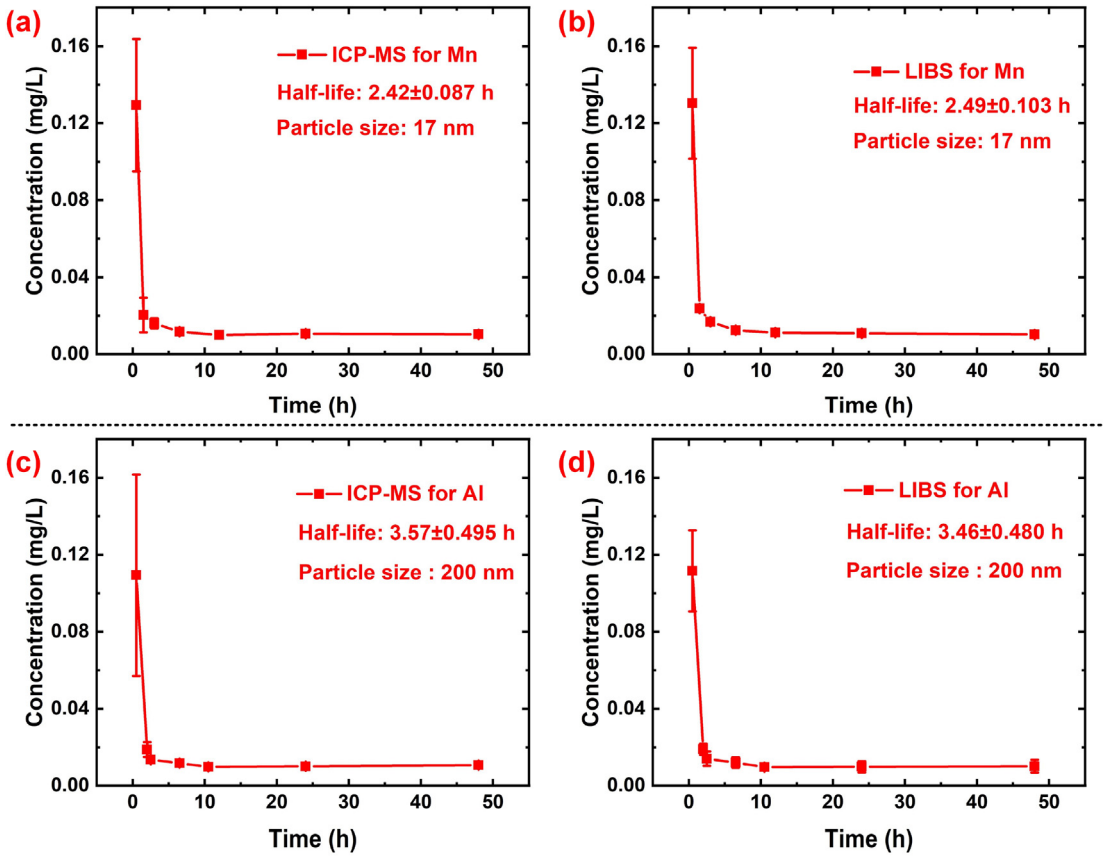

Fig. 7. The concentrations of MnO_2-BSA and AlO(OH)-BSA. (a) The half-life of MnO_2-BSA is 2.42 ± 0.087 h using ICP-MS, (b) the half-life of MnO_2-BSA is 2.49 ± 0.103 h using LIBS, (c) the half-life of AlO(OH)-BSA is 3.57 ± 0.495 h using ICP-MS, and (d) the half-life of AlO(OH)-BSA is 3.46 ± 0.480 h using LIBS.

Table 2
Comparison of quantitative analysis results between LIBS and ICP-MS.

	ICP-MS-Mn (mg/l)	LIBS-Mn (mg/l)	ICP-MS-Al (mg/l)	LIBS-Al (mg/l)
0.5 h	0.1293 ± 0.0344	0.1304 ± 0.0288	0.1094 ± 0.0524	0.1116 ± 0.0211
2.0 h	0.0203 ± 0.0090	0.0237 ± 0.0004	0.0188 ± 0.0038	0.0190 ± 0.0029
2.5 h	0.0160 ± 0.0026	0.0168 ± 0.0007	0.0136 ± 0.0015	0.0141 ± 0.0038
6.5 h	0.0117 ± 0.0015	0.0124 ± 0.0009	0.0117 ± 0.0015	0.0120 ± 0.0027
10.5 h	0.0100 ± 0.0000	0.0112 ± 0.0006	0.0098 ± 0.0007	0.0096 ± 0.0015
24.0 h	0.0107 ± 0.0006	0.0109 ± 0.0010	0.0101 ± 0.0007	0.0098 ± 0.0030
48.0 h	0.0103 ± 0.0015	0.0103 ± 0.0015	0.0107 ± 0.0013	0.0101 ± 0.0033

0.088, respectively. The mean relative errors of both MnO_2-BSA and AlO(OH)-BSA at seven time points between the results of LIBS and ICP-MS are 5.65% and 2.63%, respectively. The results show that LIBS can meet the detection accuracy for nanomaterial quantitative analyses. The half-lives of MnO_2-BSA and AlO(OH)-BSA using ICP-MS are 2.42 and 3.57 h, respectively. For LIBS, the half-lives of MnO_2-BSA and AlO(OH)-BSA are 2.49 and 3.46 h, respectively. From the results, MnO_2-BSA has a shorter half-life due to the smaller particle size than AlO(OH)-BSA. The results demonstrate that LIBS can achieve fast, low-cost, and precise detection of the metabolic rates of MnO_2-BSA and AlO(OH)-BSA. Therefore, our work provides a new way of detecting the half-lives of drugs with metal elements.

Funding

The work was supported by the National Key R&D Program of China (Grant No. 2018YFA0702100).

Compliance with ethics requirements

All animal studies were performed in compliance with protocols that had been approved by the Hubei Provincial Animal Care and Use Committee, in accordance with the experimental guidelines of the Animal Experimentation Ethics Committee of the HUST (IORG No: IORG0003571).

Declaration of Competing Interest

The authors declare that there are no conflicts of interest related to this article.

References

[1] Mukai H, Hatanaka K, Yagi N, et al. Pharmacokinetic evaluation of liposomal nanoparticle-encapsulated nucleic acid drug: A combined study of dynamic pet imaging and lc/ms/ms analysis. J Control Release 2019;294:185–94. https://doi.org/10.1016/j.jconrel.2018.12.006.

[2] Morsi NM, Aboelwafa AA, Dawoud MHS. Improved bioavailability of timolol maleate via transdermal transfersomal gel: Statistical optimization, characterization, and pharmacokinetic assessment. J Adv Res 2016;7:691–701. https://doi.org/10.1016/j.jare.2016.07.003.

[3] Seidel D, Rothe R, Kirsten M, et al. A multidimensional impedance platform for the real-time analysis of single and combination drug pharmacology in patient-derived viable melanoma models. Biosens Bioelectron 2019;123:185–94. https://doi.org/10.1016/j.bios.2018.08.049.

[4] Kontermann RE. Strategies for extended serum half-life of protein therapeutics. Curr Opin Biotechnol 2011;22:868–76. https://doi.org/10.1016/j.copbio.2011.06.012.

[5] Olsen GW, Burris JM, Ehresman DJ, et al. Half-life of serum elimination of perfluorooctanesulfonate, perfluorohexanesulfonate, and perfluorooctanoate in retired fluorochemical production workers. Environ Health Perspect 2007;115:1298–305. https://doi.org/10.1289/ehp.10009.

[6] Tian R, Long X, Yang Z, et al. Formation of a bovine serum albumin diligand complex with rutin and single-walled carbon nanotubes for the reduction of cytotoxicity. Biophys Chem 2020;256:. https://doi.org/10.1016/j.bpc.2019.106268106268.

[7] Mathew A, Sajanlal PR, Pradeep T. A fifteen atom silver cluster confined in bovine serum albumin. J Mater Chem 2011;21:11205–12. https://doi.org/10.1039/C1JM11452B.

[8] Sleep D, Cameron J, Evans LR. Albumin as a versatile platform for drug half-life extension. Biochim Biophys Acta (BBA)-General Subj 2013;1830:5526–34. https://doi.org/10.1016/j.bbagen.2013.04.023.

[9] Akbarian S, Najafpour MM, Kompany-Zareh M. Parafac study of bovine serum albumin conformational changes in the interaction with nanosized manganese oxide as a biomimetic model for water-oxidizing complex. Int J Hydrogen Energy 2017;42:9733–43. https://doi.org/10.1016/j.ijhydene.2017.02.209.

[10] Najafpour MM, Sedigh DJ, King'ondu CK, et al. Nano-sized manganese oxide–bovine serum albumin was synthesized and characterized. It is promising and biomimetic catalyst for water oxidation. RSC Adv 2012;2:11253–7. https://doi.org/10.1039/C2RA21251J.

[11] Liu H, Hu Y, Sun Y, et al. Co-delivery of bee venom melittin and a photosensitizer with an organic-inorganic hybrid nanocarrier for photodynamic therapy and immunotherapy. ACS Nano 2019;13:12638–52. https://doi.org/10.1021/acsnano.9b04181.

[12] Clases D, Birka M, Sperling M, et al. Isobaric dilution analysis as a calibration tool for long lived radionuclides in icp-ms. J Trace Elem Med Biol 2017;40:97–103. https://doi.org/10.1016/j.jtemb.2017.01.002.

[13] Gammelgaard B, Hansen HR, Stürup S, et al. The use of inductively coupled plasma mass spectrometry as a detector in drug metabolism studies. Expert Opin Drug Metab Toxicol 2008;4:1187–207. https://doi.org/10.1517/17425255.4.9.1187.

[14] Podust VN, Balan S, Sim B-C, et al. Extension of in vivo half-life of biologically active molecules by xten protein polymers. J Control Release 2016;240:52–66. https://doi.org/10.1016/j.jconrel.2015.10.038.

[15] Morrison JG, White P, McDougall S, et al. Validation of a highly sensitive icp-ms method for the determination of platinum in biofluids: application to clinical pharmacokinetic studies with oxaliplatin. J Pharm Biomed Anal 2000;24:1–10. https://doi.org/10.1016/S0731-7085(00)00377-0.

[16] Chu Y, Chen T, Chen F, et al. Discrimination of nasopharyngeal carcinoma serum using laser-induced breakdown spectroscopy combined with an extreme learning machine and random forest method. J Anal At Spectrom 2018;33:2083–8. https://doi.org/10.1039/C8JA00263K.

[17] Hermann Jr, Axente E, Pelascini F, et al. Analysis of multi-elemental thin films via calibration-free laser-induced breakdown spectroscopy. Anal Chem 2019;91:2544–50. https://doi.org/10.1021/acs.analchem.8b05780.

[18] Wu J, Liu Y, Cui Y, et al. A laser-induced breakdown spectroscopy-integrated lateral flow strip (libs-lfs) sensor for rapid detection of pathogen. Biosens Bioelectron 2019;142:. https://doi.org/10.1016/j.bios.2019.111508111508.

[19] Guo Y, Deng L, Yang X, et al. Wavelet-based interference correction for laser-induced breakdown spectroscopy. J Anal At Spectrom 2017;32:2401–6. https://doi.org/10.1039/C7JA00204A.

[20] Yi R, Li J, Yang X, et al. Spectral interference elimination in soil analysis using laser-induced breakdown spectroscopy assisted by laser-induced fluorescence. Anal Chem 2017;89:2334–7. https://doi.org/10.1021/acs.analchem.6b03969.

[21] Andersen M-BS, Frydenvang J, Henckel P, et al. The potential of laser-induced breakdown spectroscopy for industrial at-line monitoring of calcium content in comminuted poultry meat. Food Control 2016;64:226–33. https://doi.org/10.1016/j.foodcont.2016.01.001.

[22] Bilge G, Velioglu HM, Sezer B, et al. Identification of meat species by using laser-induced breakdown spectroscopy. Meat Sci 2016;119:118–22. https://doi.org/10.1016/j.meatsci.2016.04.035.

[23] Chu YW, Tang SS, Ma SX, et al. Accuracy and stability improvement for meat species identification using multiplicative scatter correction and laser-induced breakdown spectroscopy. Opt Express 2018;26:10119–27. https://doi.org/10.1364/OE.26.010119.

[24] Amodeo T, Dutouquet C, Tenegal F, et al. On-line monitoring of composite nanoparticles synthesized in a pre-industrial laser pyrolysis reactor using laser-induced breakdown spectroscopy. Spectrochim Acta, Part B 2008;63:1183–90. https://doi.org/10.1016/j.sab.2008.09.005.

[25] Yuan R, Tang Y, Zhu Z, et al. Accuracy improvement of quantitative analysis for major elements in laser-induced breakdown spectroscopy using single-sample calibration. Anal Chim Acta 2019;1064:11–6. https://doi.org/10.1016/j.aca.2019.02.056.

[26] Choi J-J, Choi S-J, Yoh JJ. Standoff detection of geological samples of metal, rock, and soil at low pressures using laser-induced breakdown spectroscopy. Appl Spectrosc 2016;70:1411–9. https://doi.org/10.1177/0003702816664858.

[27] Michel AP, Sonnichsen F. Laser induced breakdown spectroscopy for heavy metal detection in a sand matrix. Spectrochim Acta, Part B 2016;125:177–83. https://doi.org/10.1016/j.sab.2016.10.001.

[28] Chen Z, Li H, Liu M, et al. Fast and sensitive trace metal analysis in aqueous solutions by laser-induced breakdown spectroscopy using wood slice substrates. Spectrochim Acta, Part B 2008;63:64–8. https://doi.org/10.1016/j.sab.2007.11.010.

[29] Lee Y, Oh S-W, Han S-H. Laser-induced breakdown spectroscopy (libs) of heavy metal ions at the sub-parts per million level in water. Appl Spectrosc 2012;66:1385–96. https://doi.org/10.1366/12-06639R.

[30] Shi H. Measurement of trace heavy metal zinc in water by laser induced breakdown spectroscopy. Laser Optoelectron Prog 2012;49:. https://doi.org/10.3788/LOP49.013003013003.

[31] Zhao F, Chen Z, Zhang F, et al. Ultra-sensitive detection of heavy metal ions in tap water by laser-induced breakdown spectroscopy with the assistance of electrical-deposition. Anal Methods 2010;2:408–14. https://doi.org/10.1039/B9AY00160C.

[32] Aguirre MA, Legnaioli S, Almodóvar F, et al. Elemental analysis by surface-enhanced laser-induced breakdown spectroscopy combined with liquid–liquid microextraction. Spectrochim Acta, Part B 2013;79–80:88–93. https://doi.org/10.1016/j.sab.2012.11.011.

[33] Samek O, Beddows DC, Kaiser J, et al. Application of laser-induced breakdown spectroscopy to in situ analysis of liquid samples. Opt Eng 2000;39:2248–62. https://doi.org/10.1117/1.1304855.

[34] Yueh F-Y, Sharma RC, Singh JP, et al. Evaluation of the potential of laser-induced breakdown spectroscopy for detection of trace element in liquid. J Air Waste Manag Assoc 2002;52:1307–15. https://doi.org/10.1080/10473289.2002.10470860.

[35] Chang C-C, Lin C-J. Libsvm: A library for support vector machines. ACM Trans Intell Syst Technol (TIST) 2011;2:27. https://doi.org/10.1145/1961189.1961199.